Unexpected consequences of transverse isotropy

Hitoshi Kawakatsu[1]
[1]Earthquake Research Institute, The University of Tokyo, Japan

October 7, 2020

Abstract

In a series of papers, Kawakatsu et al. (2015) and Kawakatsu (2016a,b, 2018) introduced and discussed a new parameter, η_κ, that characterizes the incidence angle dependence (relative to the symmetry axis) of seismic body wave velocities in a transverse isotropy (TI) system. During the course of these exercises, several nontrivial consequences of transverse isotropy are realized and summarized as follows: (1) P-wave velocity (anisotropy) strongly influences the conversion efficiency of P-to-S and S-to-P, as much as S-wave velocity perturbation does; (2) Rayleigh wave phase velocity has substantial sensitivity to P-wave anisotropy near the surface; (3) a trade-off exists between η_κ and Vp/Vs-ratio if the latter is sought under an assumption of isotropy or the elliptic condition. Among these findings, the first two deserve careful attention in interpretation of results of popular seismic analysis methods, such as receiver function analysis and ambient noise Rayleigh wave dispersion analysis. We present simple example cases for such problems to delineate the effect in actual situations, as well as scalings among TI parameters of the crust and mantle materials or models that might help understanding to what extent the effect becomes important.

Introduction

Kawakatsu (2018) recently showed that reflection and transmission of plane waves in a transversely isotropic system with a vertical symmetry axis (VTI) had unexpected properties by the analogy of the corresponding isotropic case: P-wave speed (anisotropy) strongly influences the conversion efficiency of P-to-S and S-to-P, as much as S-wave speed perturbation does. It was also pointed out that, with the properly defined set of VTI parameters using the new fifth parameter, η_κ, Rayleigh-wave phase velocity had substantial increased sensitivity to the shallowmost P-wave anisotropy, especially near the surface, although the sensitivity is generally much reduced elsewhere. This suggests that P-wave anisotropy might have significant consequences for the interpretation of receiver functions and/or ambient noise Rayleigh wave dispersion measurements that are now commonly employed in crustal and mantle studies of shear velocity. The purpose of this short note is to present such example case waveforms for receiver function analysis and Rayleigh wave sensitivity kernels for 1-D VTI structures to draw attention of researchers in the related field.

Representation of VTI or radial anisotropy

In a VTI, or equivalently radial anisotropy, system, horizontally and vertically propagating P-waves have phase velocities of

$$\alpha_H = \sqrt{A/\rho} \tag{1}$$

and

$$\alpha_V = \sqrt{C/\rho}, \tag{2}$$

respectively, where ρ gives the density. As for shear waves, horizontally and vertically polarized *horizontally propagating S-waves* respectively have phase velocities of

$$\beta_H = \sqrt{N/\rho} \tag{3}$$

and

$$\beta_V = \sqrt{L/\rho}, \tag{4}$$

and *vertically propagating S-waves* also have a phase velocity of β_V (*cf*. Figure 1 of Kawakatsu (2016a)). So for these horizontally or vertically traveling bodywaves, phase velocities are given by the four elastic constants, A, C, L and N, and the ratios of these elastic constants define the degree of radial anisotropy,

$$\varphi^{-1} = A/C = \alpha_H^2/\alpha_V^2 \tag{5}$$

for the P-wave, and

$$\xi = N/L = \beta_H^2/\beta_V^2 \tag{6}$$

for the S-wave (Takeuchi and Saito, 1972). As for the P-wave anisotropy index, we specifically use φ^{-1}, because for many of realistic cases, the strength of anisotropy for P and S is positively correlated, and also because having α_V as a reference (i.e., denominator) is more reasonable for a layered VTI medium as in Thomsen's parameters (Thomsen, 1986). For other intermediate direction bodywaves, the fifth elastic constant, F, affects the incidence angle dependence of quasi-P and quasi-SV waves via η_κ,

$$\eta_\kappa \;=\; \frac{(F+L)}{(A-L)^{1/2}(C-L)^{1/2}}, \tag{7}$$

(Kawakatsu, 2016a).

Synthetic waveform examples: Ps or Sp conversion without S-wave speed perturbation

We consider the elastic response (noise free) of a homogeneous layer (80 km thick) over a homogeneous half-space to incident P or S plane waves. As for a reference isotropic case, the upper layer is given by a Poisson solid whose P-wave and S-wave velocities and density are given by $\alpha_1 = 8.0\,km\,s^{-1}$, $\beta_1 = 4.6188\,km\,s^{-1}$, and $\rho_1 = 3.3\,g\,cc^{-1}$, and the lower half-space with 5% velocity reduction for S, but not for P and density. As for anisotropic cases, for the sake of simplicity, we introduce anisotropy only for the lower layer. We employ anisotropy strength, a_p and a_s, to specify anisotropic velocities as

$$\alpha_{H/V} = \alpha_0(1 \mp a_p/2), \quad \beta_{H/V} = \beta_0(1 \mp a_s/2),$$

where $\alpha_0 = (\alpha_V + \alpha_H)/2$ and $\beta_0 = (\beta_V + \beta_H)/2$ denote reference isotropic wave speeds, and $a_p = (\alpha_V - \alpha_H)/\alpha_0$, $a_s = (\beta_V - \beta_H)/\beta_0$. Also for the sake of simplicity, we assume the elliptic condition (i.e., $\eta_\kappa = 1.0$) in which a phase slowness surface of P-wave becomes elliptic (Kawakatsu, 2016a). It should be also noted that S-wave anisotropy itself does not directly enter in the P/SV coupling in VTI, and thus the effect of changing it is equivalent to that of changing the S-wave speed, β_V.

In Figure 1a, instead of receiver functions, we show radial component waveforms at a surface point of the top layer; as for the waveform for the primary P-S conversion phase, the isotropic case (thin line) with 5% S-speed reduction is almost identical to the anisotropic case with $a_p = 5\%$ (thick line), while one with $a_p = -5\%$ (broken line) exhibits reversed polarity. For anisotropic cases, the situation is consistent with the properties of the transmission coefficients described in Kawakatsu (2018): An S-wave speed reduction of 5% generates a converted phase nearly equivalent to that caused by P-wave anisotropy of $a_p = 5\%$, which makes α_V (α_H) 2.5% faster (slower) than the reference velocity, α_0. For the secondary multiples, the situation is different, indicating a possibility of differentiating the effects of S-wave speed and P-wave anisotropy. A similar observation can be made for the case of the S-wave incidence; in Figure 1b, the vertical component of S-wave waveforms that is used for S-receiver function is shown. The precursors to S, i.e., Sp, show similar behavior to Ps for P-wave case; i.e., the significant effect of P anisotropy on S-to-P conversion can be seen. It should be noted that the amplitudes in Figure 1 depend on the slowness of incoming plane waves, and will vary differently with ray parameter depending on the arrival type (primary conversions vs. multiples, etc.). The ray parameter of $0.06 s/km$ employed for the synthetic waveforms presented in Figure 1a,c is a typical one for the teleseismic P-wave case ($0.04 - 0.08\, s/km$). The ray parameter of $0.09 s/km$ for the S-wave incidence case (Figure 1b,d) corresponds to the lower end of the teleseismic range ($0.09 - 0.12\, s/km$). Although the amplitudes of the primary conversion phases (Ps and Sp), which are the main focus of the present manuscript, vary depending on the employed ray parameter within the teleseismic range, the significant effect of P-anisotropy compared to that of the S-wave speed reduction discussed above is unchanged.

Significance of P-wave anisotropy in receiver function analysis

It is well known for isotropic material that P-to-S and S-to-P conversions have a strong sensitivity to S-wave speed perturbation and a weak one to density (note however that multiples have a higher sensitivity to density contrasts), but no sensitivity to P-wave speed in the first order (e.g., Aki and Richards, 1980). Based on this, in most of receiver function analyses, we generally assume the primary converted phases to represent the structure of the S-wave speed perturbation. Kawakatsu (2018), on the other hand, showed that once anisotropy (TI) was considered, P-wave anisotropy was as important as S-wave structure, and in this report, we present simple 1-D examples of converted waveforms without S-wave perturbations (Figure 1).

Figure 1 indicates that P-anisotropy of +5% ($a_p = 0.05$) gives comparable amplitude of Ps (or Sp) phase to S-wave speed reduction of 5% ($\Delta\beta_V = -5\%$). Note that radial anisotropy on the order of 5% or larger has been reported for the oceanic crust (Russell et al., 2019) and the mantle (asthenosphere) (e.g., Nettles and Dziewonski, 2008) and 10% $\sim$ 30% beneath active volcanos (Jaxybulatov et al., 2014;

Nagaoka, 2020). To examine a more realistic situation, let us consider a case of fabrics representing the mantle. It is generally known that P and S anisotropy correlates positively for mantle fabrics (e.g., Montagner and Anderson, 1989; Becker et al., 2006). Consider a case that the strength of P and S-wave anisotropy is comparable (i.e., $a_p \sim a_s$, $\varphi^{-1} \sim \xi$); then P-anisotropy of -5% means S-anisotropy of -5%, equivalent to $\Delta\beta_V = -2.5\%$ in the case of Figure 1. Therefore, the contributions of P- and S-anisotropy to the Ps phase are opposite in sign, and the P-anisotropy contribution dominates. This is somewhat paradoxical, but it is the case: i.e., when β_V decreases, the corresponding receiver function shows a positive primary Ps phase if it is due solely to the fabric. Thus, in environments where seismic anisotropy is important, the interpretation of receiver functions may require careful attention (e.g., Moho, MLD (mid-lithospheric discontinuity), or LAB (lithosphere-asthenosphere boundary); Brownlee et al. (2017); Abt et al. (2010); Kawakatsu et al. (2009), respectively).

Rayleigh wave sensitivity to near-surface P-anisotropy

A small change in phase velocity (c) of surface waves at a given angular frequency (ω) due to changes in material properties can be expressed as,

$$\left(\frac{\delta c}{c}\right)_\omega = \sum_i \int K_{\epsilon_i}(z) \left(\frac{\delta \epsilon_i}{\epsilon_i}\right) dz, \tag{8}$$

where ϵ_i denotes the i-th elastic parameter among five anisotropy parameters of VTI or the density at a depth z, and $K_{\epsilon_i} = \frac{\epsilon_i}{c}\left[\frac{\partial c}{\partial \epsilon_i}\right]_\omega$ represents the corresponding sensitivity kernel (partial derivative) (e.g., Takeuchi and Saito, 1972; Aki and Richards, 1980). For Rayleigh waves, when we use the set $(\alpha_H, \alpha_V, \beta_H, \beta_V, \eta_\kappa\, or\, \eta)$ as parameters, where $\eta = F/(A-2L)$ is the conventional fifth parameter defined by Takeuchi and Saito (1972), the explicit expressions for K_{ϵ_i}'s are given in Kawakatsu (2016b). The influence of P-anisotropy change on c can be written as

$$\begin{aligned} \left(\frac{\delta c}{c}\right)_\omega &= \int \left\{ K_{\alpha_V}(z)\left(\frac{\delta\alpha_V}{\alpha_V}\right) + K_{\alpha_H}(z)\left(\frac{\delta\alpha_H}{\alpha_H}\right)\right\} dz \\ &= \int \left\{ (K_{\alpha_V} + K_{\alpha_H})\left(\frac{\delta\alpha_0}{\alpha_0}\right) + \left(\frac{K_{\alpha_V} - K_{\alpha_H}}{2}\right)\delta a_p \right\} dz, \end{aligned} \tag{9}$$

assuming the initial unperturbed state is isotropic, i.e., $\alpha_V = \alpha_H = \alpha_0$.

Kawakatsu (2016b) pointed out that, with the introduction of the properly defined set of VTI parameters with η_κ, the Rayleigh wave sensitivity kernel to P-anisotropy was significantly modified and that some of the previously claimed sensitivity (Dziewonski and Anderson, 1981; Anderson and Dziewonski, 1982) was an inappropriate projection of the sensitivity of S-anisotropy into that of P-anisotropy. Figure 2 shows such Rayleigh wave sensitivity kernels with the new parameters using the expression (9) at the peak period of the microseisms (7 s), which are now commonly used to infer the subsurface structure via ambient noise dispersion analysis (e.g., Shapiro and Campillo, 2004; Nishida et al., 2008). The P-anisotropy kernel (a_p) shows a sharp increase in sensitivity (i.e., the absolute amplitude) near the surface (from nearly zero at a depth of $2.5\,km$ to $|-0.08|$ at $0\,km$), although the amplitude is generally reduced elsewhere. For the top $2\,km$, the sensitivity to a_p is as large as that to β_V. Considering that $\delta\beta_V \sim a_s/2$, this indicates that the sensitivity to P-anisotropy is nearly twice as large as that to S-anisotropy and the sign is opposite; this characteristic is quite similar to that of P-S and S-P conversions discussed earlier and appears to indicate that the increase of P-anisotropy sensitivity near the surface is related to P-S and S-P conversions at the free surface.

This may affect the interpretation of ambient noise tomography (e.g., Lin et al., 2010), as well as time-lapse measurements of phase velocity (e.g., Brenguier et al., 2008a,b; Nishida et al., 2020). For example, introducing P-anisotropy of $a_p = 5\%$ (while keeping β_V and η_κ constant, but not η that is essential (Kawakatsu, 2016b)) for the top $2.25km$ of the model in Figure 2 (i.e., flat PREM without water layer) will decrease the phase velocity about 0.37%. This value is about one order of magnitude larger than those observed in pre-eruption phases at the Piton de la Fournaise volcano (Brenguier et al., 2008b) and Shinmoe-dake of the Kirishima volcano (Nishida et al., 2020), and post-seismically in Parkfield (Brenguier et al., 2008a). That is, a change of near-surface P-anisotropy of $a_p \sim 0.5\%$ that might be caused by, for example, opening or healing of cracks (e.g., Crampin, 1984), could potentially explain those observations. Figure 2 indicates that the sensitivities of the Rayleigh wave phase velocity to near-surface a_p and a_s (β_V) are opposite in sign; i.e., if P and S-anisotropy are positively correlated, the near-surface net effect tends to cancel each other depending on the degree of the correlation; in case they are linearly correlated as discussed for the case of P-S conversion before, the effect of P-anisotropy dominates the phase velocity change. Therefore, if anisotropy becomes an important factor, the interpretation might not be straightforward.

Trade-off between η_κ and Vp/Vs ratio

The incidence angle dependence of quasi P- and Sv-wave phase velocities on η_κ indicates that the effect is opposite between P and Sv; i.e., in the propagation direction where P velocity increases, Sv velocity decreases and vice versa (Figure 3). This suggests that if this effect is ignored (i.e., if the elliptic condition or isotropy is assumed), the estimate of Vp/Vs-ratio can be biased. The spherical average of this effect can be estimated under the assumption of weak anisotropy as

$$\frac{\overline{V_P}}{\overline{V_{SV}}} \approx \frac{\alpha_v}{\beta_v}\left(1-\frac{8}{45}\sigma\right) \approx \frac{\alpha_v}{\beta_v}\left[1+\frac{16}{45}(\eta_\kappa-1)\right] \tag{10}$$

where, using Thomsen parameters, the following approximation is employed,

$$\begin{aligned}\sigma &= \frac{\alpha_V^2}{\beta_V^2}(\varepsilon-\delta) = \frac{1}{2}\left(1-\eta_\kappa^2\right)\left(\frac{A}{L}-1\right)\\ &\approx \left(1-\eta_\kappa^2\right) \approx -2(\eta_\kappa-1) \quad (\text{if } A\approx 3L),\end{aligned} \tag{11}$$

where σ follows the definition of Tsvankin and Thomsen (1994) (cf. Kawakatsu, 2018) and is not Poisson's ratio. So the effect of this bias roughly scales with one third of $(\eta_\kappa - 1)$ if a Poisson solid-type character is assumed. If η_κ lies between 0.9 and 1.1 as seen in later examples, the Vp/Vs-ratio bias will be less than $\sim \pm 3.5\,\%$ and might not be so significant except for some peculiar situations, such as laminated melt layering (*cf.* Figure 4) or SPO (shape-preferred orientation) of volatile-filled high aspect ratio cracks under shear.

It may be informative to compare (10) with ratios of $V_P(45)$ to $V_P(0)$ and $V_{SV}(45)$ to $V_{SV}(0)$ (numbers in parentheses denote incidence angles measured from the symmetry axis) (e.g., Okaya and Christensen, 2002) that measure the strength of the 4θ term of anisotropy. Assuming the absence of P-anisotropy (i.e., $A = C$ and $\varphi^{-1} = 1$), it can be shown that

$$\frac{\hat{V}_P(45)}{\hat{V}_P(0)} = \left[1+\frac{1-L/C}{2}(\eta_\kappa-1)\right]^{1/2} \approx 1+\frac{1}{6}(\eta_\kappa-1) \tag{12}$$

and

$$\frac{\hat{V}_{SV}(45)}{\hat{V}_{SV}(0)} = \left[1+\frac{1-C/L}{2}(\eta_\kappa-1)\right]^{1/2} \approx 1-\frac{1}{2}(\eta_\kappa-1) \tag{13}$$

where $\hat{}$ denotes the absence of P-anisotropy.

Discussion

Scaling among VTI parameters

Mantle In order to find out to what extent discussed consequences of VTI impact on actual geophysical interpretation, understanding of the scaling among VTI parameters might be useful. Here we compare two end-member scenarios for the mantle: olivine crystal-preferred orientation (CPO) fabrics and the laminated melt structure (*millefeuille* (MF) model). For the former, we assume that the crystallographic b-axis is aligned in the vertical direction and its azimuthal (Montagner) average (Montagner and Nataf, 1986; Chen and Tromp, 2007) is considered for various fabrics (Saruwatari et al., 2001; Jung et al., 2006; Ohuchi et al., 2011; Michibayashi et al., 2016). For the latter, we employ a layered melt parameterization of Kawakatsu et al. (2015); we construct a series of VTI models by Backus averaging (Backus, 1962) of a stack of two kinds of homogeneous isotropic layers: soft layers embedded in a background solid matrix (e.g., Kawakatsu et al., 2009). We parameterize (i) the proportional reduction of rigidity of soft layers to the background by a ($0 \leq a \leq 1$), (ii) the proportional reduction of the bulk modulus by $a/2$, and (iii) the volume fraction of soft layers by f ($0 \leq f \leq 1$). Figure 4 shows the correlation among VTI parameters for such models. In case of reported CPO fabrics (both natural and laboratory) there exists a strong positive scaling between S and P wave anisotropy, while for the millefeuille model S-anisotropy dominates:

$$\varphi^{-1} \sim \xi^{1.0-1.5} \quad \text{(for olivine)}$$

$$\varphi^{-1} \sim \xi^{0.2} \quad \text{(for millefeuille).}$$

These two end-member models represent very different behavior for receiver functions. For the millefeuille model, as the dependence on P-anisotropy is weak, the S-wave speed effect dominates the receiver functions. On the other hand for the olivine case, as we discussed earlier, the P-anisotropy effect dominates. As the scaling index ranges roughly from 1 to 1.5, the discussed dominance of P-anisotropy could be even more significant than previously considered. In Figure 5(a), we show synthetic waveforms, as in Figure 1, for some of the representative fabric models (A-, B-, C-, and E-type olivine of Jung et al. (2006)) for the lower anisotropic half space; we set the reference velocities (α_0, β_0) of the lower layer equal to that of the surface layer. Then, we use anisotropy parameters of the models to construct the equivalent anisotropy lower layer (Table 1). For example, a case of A-type olivine of Jung et al. (2006), which has strong P-anisotropy ($a_p = -3.9\%$) and mild S-anisotropy ($a_s = -1.6\%$) for azimuthally averaged VTI, shows a positive primary phase, while the C-type olivine ($a_p = +2.7\%$, $a_s = +2.2\%$) case shows negative one. Compared to the case of 5 % S-velocity decreases, these particular olivine fabrics affect the Ps-phase amplitude about half or less. For the MF model, model parameters are $a = 0.92$ and $f = 0.01$ that give $a_p = -0.6\%$, $a_s = -5.0\%$, and $\eta_\kappa = 0.92$. The absolute amplitude of the primary Ps-phase is as large as that of the $\Delta\beta_V = -5\%$ case, but half of the contribution comes from the η_κ effect (*cf.* Figure 2b of Kawakatsu (2018)). In reality, two end-member models may co-exist and other isotropic effects, such as temperature, may take roles that further complicate the interpretation. Also, VTI could be just an azimuthal average of more general anisotropy. Therefore, for environments where seismic anisotropy is important, the interpretation of receiver functions may require careful attention.

It may be of interest to comment on the scaling between S (or P) anisotropy and the fifth parameter, η_κ. For the millefeuille case, a clear scaling,

$$\eta_\kappa \sim \xi^{-0.8}$$

emerges, resulting in $\eta_\kappa < 1$. While the natural olivine samples representing the lithospheric mantle (Michibayashi et al., 2016) show scaling $\eta_\kappa \sim \xi^{-0.4}$, other fabrics show more scattered behavior. Notably, some mantle xenoliths exhibit $\eta_\kappa \sim 1.03$, comparable to the value suggested for the oceanic asthenosphere by Song and Kawakatsu (2012, 2013) to explain the trench-parallel fast direction of the sub-slab anisotropy (Long and Silver, 2008) as a simple consequence of the geometrical effect of tilted transverse isotropy (TTI) at subduction zones.

Crust Figure 6 presents correlation among the VTI parameters for the crustal fabrics reported by Brownlee et al. (2017). Considering the possibility of complex fabrics orientation in a crust setting, here we construct a series of VTI models for each fabric given by azimuthal averaging (Montagner and Nataf, 1986) of an arbitrarily rotated elastic tensor (the rotation is done with a 30-degree interval for each Euler angle that results in 72 (12×6; rotation around the original z-axis can be azimuthally averaged out) VTI models for each original fabric). Among the various rock-types classified in Brownlee et al. (2017), those fabrics grouped as “amphibolite” indicate clear correlations of the VTI parameters

(Figure 6a); the trend is generally similar to that for the mantle fabrics shown in Figure 4, but with stronger anisotropy (1.5 $\sim$ 2 times), and thus a similar qualitative argument for the impact of the VTI on the receiver functions can be made. As for the rest of fabrics, points are more scattered but still somewhat similar correlations appear to emerge (*cf.* Supplemental Material). Those consisting of significant mica component ($>10\%$) can have very strong anisotropy (ξ or φ^{-1} up to 1.8; *cf.* Figures S2,S4). Considering that the S-velocity increase at Moho is $\sim 15\%$, $a_p \sim \pm 15\,\%$ (i.e., $\varphi^{-1} \sim 1.0 \mp 0.3$) could have comparable effect. So these fabrics could potentially impact on the interpretation of receiver function signals from Moho.

To model a more realistic Moho structure, we simulate radial component seismograms for a P-wave incidence into an interface at a depth of 80 km with a $\sim 15\,\%$ S-velocity increase (Figure 5(b)). The thick dark solid line represents a reference case where both layers are isotropic: the amplitude of Ps phase is $\sim 10\,\%$ of that of the direct P-wave. When we introduce P-anisotropy of $a_p = -7.5\,\%$ ($\varphi^{-1} \sim 1.15$) in the upper crustal layer, the Ps amplitude is reduced about half as expected from the above argument (thin broken line). Instead, if we introduce radial anisotropy equivalent of A-type olivine (generally believed to be the most dominant fabric in the mantle; Table 1) in the lower layer, the Ps amplitude increases about 30 % (thick medium line). We compare this with three additional cases in which the upper layer has P-anisotropy of $a_p = -7.5\,\%$ and S-anisotropy of $a_s = 0\,\%, -5\,\%, -7.5\,\%$, respectively representing a pure P-anisotropy case and two different scaling of $\varphi^{-1} \sim \xi^{1.5}$ and $\varphi^{-1} \sim \xi^{1.0}$. Here, the reduction of the Ps amplitude ranges from $\sim 40\,\%$ to $\sim 15\,\%$, and the decrease of the reduction is due to the competing effect of the P and S anisotropy. The range of the Ps amplitude variation exemplified here is larger than the uncertainty of the S-wave velocity jump at the continental Moho estimated from the array stacked receiver functions (e.g., Niu and James, 2002). Therefore, crustal P-anisotropy discussed here should have observable effects on P-wave receiver functions. As for other discontinuities with smaller velocity changes, such as LAB or MLD, the relative significance of P-anisotropy could be more severe depending on the actual situation.

In summary, the situation for both mantle and crust could be very complicated, and invoking a probabilistic parameter space search (e.g., Mosegaard and Tarantola, 1995; Bodin et al., 2012) with appropriate *a priori* constraints might help to infer the actual structure. It should be also noted that variations with slowness and azimuth of conversion amplitudes in receiver functions may allow distinctions between isotropic S contrasts and anisotropic P contrasts.

Intrinsic *vs.* extrinsic VTI

VTI or radial anisotropy discussed in this paper represents, by definition, a hexagonally anisotropic system with the symmetry axis that is vertical. Such a system can be considered as a realization of nature in two ways: intrinsic and extrinsic VTI. Intrinsic VTI occurs when symmetry axes of hexagonal symmetry crystals are aligned vertically, or when horizontally laminated structure dominates (e.g., millefeuille). Extrinsic VTI occurs in other cases as a result of azimuthal averaging of arbitrary anisotropy. In the case of intrinsic VTI, discussions presented in this paper can be taken as they are. In the case of extrinsic VTI, the azimuthal variation of receiver functions or dispersion measurements has to be considered, and in the data analysis, azimuthal averaging is essential. It is a common practice for the Rayleigh wave dispersion analysis. On the other hand, for the receiver function analysis, how (back-)azimuthal averaging of receiver functions of arbitrary anisotropy compares with that of azimuthally averaged VTI might not be straightforward (e.g., Levin and Park, 1998) when the azimuthal anisotropy term is strong compared to the radial anisotropy one; this may deserve careful attention, but is beyond the scope for the present paper. It should be noted that in the recent analyses, strong radial anisotropy is reported in the oceanic crust and mantle (Russell et al., 2019; Nettles and Dziewonski, 2008) and beneath active volcanos (Jaxybulatov et al., 2014; Nagaoka, 2020). It is also worth mentioning that Levin and Park (1998) reported that the importance of P-anisotropy in the generation of P-to-S converted P coda waves, although anisotropy in their analysis refers to that of tilted transverse isotropy (TTI).

Conclusion

We discussed several nontrivial consequences of the wave propagation in a transverse isotropy (TI) system, and presented example cases to show the significant effect of P-wave anisotropy on both receiver function analysis and Rayleigh wave dispersion analysis. This suggests that in the presence of anisotropy, careful interpretation of receiver functions and ambient noise Rayleigh wave dispersion are required. We also presented scalings among VTI parameters of the crust and mantle materials or models that might help delineating to what extent this effect becomes important and be used in the actual problems as *a priori* constraints.

Data and Resources

No seismic data were used in this paper. Supplemental Material presents correlations among the VTI parameters for each of the crustal fabrics reported by Brownlee et al. (2017).

Acknowledgements

This research is partly supported by JSPS KAKENHI Grant Number 17H02948, 18H03735 and 19K21892. The author thanks Katsuyoshi Michibayashi and Sarah Brownlee for the natural fabric data of Michibayashi et al. (2016) and Brownlee et al. (2017), and Alex Song for discussions. He also thanks two reviewers and the associate editor for comments that significantly improved the manuscript, and particularly, Joshua Russell for thoughtful comments and questions.

References

Abt, D.L., Fischer, K.M., French, S.W., Ford, H.A., Yuan, H., Romanowicz, B., 2010. North American lithospheric discontinuity structure imaged by Ps and Sp receiver functions. J. Geophys. Res. Solid Earth 115, B09301. doi:10.1029/2009JB006914.

Aki, K., Richards, P., 1980. Quantitative Seismology: Theory and Methods. W. H. Freeman, New York.

Ammon, C.J., 1991. The isolation of receiver effects from teleseismic P waveforms. Bull. Seismol. Soc. Am. 81, 2504–2510.

Anderson, D.L., Dziewonski, A.M., 1982. Upper mantle anisotropy: evidence from free oscillations. Geophys. J. Int. 69, 383–404.

Backus, G.E., 1962. Long-wave elastic anisotropy produced by horizontal layering. J. Geophys. Res. 67, 4427–4440.

Becker, T., Chevrot, S., Schulte-Pelkum, V., Blackman, D.K., 2006. Statistical properties of seismic anisotropy predicted by upper mantle geodynamic models. J. Geophys. Res. 111, B08309. doi:10.1029/2005JB004095.

Bodin, T., Sambridge, M., Tkalcic, H., Arroucau, P., Gallagher, K., Rawlinson, N., 2012. Transdimensional inversion of receiver functions and surface wave dispersion. J. Geophys. Res. Solid Earth 117, B02301. doi:10.1029/2011JB008560.

Brenguier, F., Campillo, M., Hadziioannou, C., Shapiro, N.M., Nadeau, R.M., Larose, E., 2008a. Postseismic Relaxation Along the San Andreas Fault at Parkfield from Continuous Seismological Observations. Science 321, 1478–1481. doi:10.1126/science.1160943.

Brenguier, F., Shapiro, N.M., Campillo, M., Ferrazzini, V., Duputel, Z., Coutant, O., Nercessian, A., 2008b. Towards forecasting volcanic eruptions using seismic noise. Nature Geoscience 1, 126–130. doi:10.1038/ngeo104.

Brownlee, S.J., Schulte-Pelkum, V., Raju, A., Mahan, K., Condit, C., Orlandini, O.F., 2017. Characteristics of deep crustal seismic anisotropy from a compilation of rock elasticity tensors and their expression in receiver functions. Tectonics 36, 1835–1857. doi:10.1002/2017TC004625.

Chen, M., Tromp, J., 2007. Theoretical and numerical investigations of global and regional seismic wave propagation in weakly anisotropic earth models. Geophys. J. Int. 168, 1130–1152. doi:10.1111/j.1365-246X.2006.03218.x.

Crampin, S., 1984. Effective anisotropic elastic constants for wave propagation through cracked solids. Geophys. J. Roy. Astr. Soc. 76, 135–145. doi:10.1111/j.1365-246X.1984.tb05029.x.

Dziewonski, A.M., Anderson, D.L., 1981. Preliminary reference Earth model. Phys. Earth Planet. Inter. 25, 297–356.

Jaxybulatov, K., Shapiro, N.M., Koulakov, I., Mordret, A., Landes, M., Sens-Schonfelder, C., 2014. A large magmatic sill complex beneath the Toba caldera. Science 346, 617–619. doi:10.1126/science.1258582.

Jung, H., Katayama, I., Jian, Z., Hiraga, T., Karato, S., 2006. Effect of water and stress on the lattice-preferred orientation of olivine. Tectonophysics 421, 1–22.

Kawakatsu, H., 2016a. A new fifth parameter for transverse isotropy. Geophys. J. Int. 204, 682–685. doi:10.1093/gji/ggv479.

Kawakatsu, H., 2016b. A new fifth parameter for transverse isotropy II: partial derivatives. Geophys. J. Int. 206, 360–367. doi:10.1093/gji/ggw152.

Kawakatsu, H., 2018. A new fifth parameter for transverse isotropy III: reflection and transmission coefficients. Geophys. J. Int. 213, 426–433. doi:10.1093/gji/ggy003.

Kawakatsu, H., Kumar, P., Takei, Y., Shinohara, M., Kanazawa, T., Araki, E., Suyehiro, K., 2009. Seismic Evidence for Sharp Lithosphere-Asthenosphere Boundaries of Oceanic Plates. Science 324, 499–502.

Kawakatsu, H., Montagner, J.P., Song, T.R.A., 2015. On DLA's η, In *The Interdisciplinary Earth: A volume in honor of Don L. Anderson*. GSA and AGU. pp. 33–38.

Levin, V., Park, J., 1998. P-SH Conversions in Layered Media with Hexagonally Symmetric Anisotropy: A CookBook. Pure Appl. Geophys. 151, 669–697.

Lin, F.C., Ritzwoller, M.H., Yang, Y., Moschetti, M.P., Fouch, M.J., 2010. Complex and variable crustal and uppermost mantle seismic anisotropy in the western United States. Nature Geoscience 4, 55–61. doi:DOI: 10.1038/NGEO1036.

Long, M., Silver, P.G., 2008. The subduction zone flow field from seismic anisotropy: A global view. Science 319, 315–318. doi:10.1126/science.1150809.

Michibayashi, K., Mainprice, D., Fujii, A., Uehara, S., Shinkai, Y., Kondo, Y., Ohara, Y., Ishii, T., Fryer, P., Bloomer, S.H., Ishiwatari, A., Hawkins, J.W., Ji, S., 2016. Natural olivine crystal-fabrics in the western Pacific convergence region: A new method to identify fabric type. Earth Planet. Sci. Lett. 443, 70–80. doi:10.1016/j.epsl.2016.03.019.

Montagner, J.P., Anderson, D.L., 1989. Constraints on elastic combinations inferred from petrological models. Phys. Earth Planet. Inter. 54, 82–105.

Montagner, J.P., Nataf, H.C., 1986. On the inversion of the azimuthal anisotropy of surface waves. J. Geophys. Res. 91, 511–520.

Mosegaard, K., Tarantola, A., 1995. Monte Carlo sampling of solutions to inverse problems. J. Geophys. Res. 100, 12–431.

Nagaoka, Y., 2020. Study on seismic velocity structure beneath active volcanoes by seismic interferometry. Ph.D. Thesis, The university of Tokyo.

Nettles, M., Dziewonski, A.M., 2008. Radially anisotropic shear velocity structure of the upper mantle globally and beneath North America. J. Geophys. Res. 113, B02303. doi:10.1029/2006JB004819.

Nishida, K., Kawakatsu, H., Obara, K., 2008. Three-dimensional crustal S wave velocity structure in Japan using microseismic data recorded by Hi-net tiltmeters. J. Geophys. Res. 113, B10302. doi:10.1029/2007JB005395.

Nishida, K., Mizutani, Y., Ichihara, M., Aoki, Y., 2020. Time-lapse monitoring of seismic velocity associated with 2011 Shinmoe-dake eruption using seismic interferometry: An extended Kalman filter approach. J. Geophys. Res. Solid Earth 125, e2020JB020180. doi:10.1029/2020JB020180.

Niu, F., James, D.E., 2002. Fine structure of the lowermost crust beneath the Kaapvaal craton and its implications for crustal formation and evolution. Earth Planet. Sci. Lett. 200, 121–130. doi:10.1016/S0012-821X(02)00584-8.

Ohuchi, T., Kawazoe, T., Nishihara, Y., Nishiyama, N., Irifune, T., 2011. High pressure and temperature fabric transitions in olivine and variations in upper mantle seismic anisotropy. Earth Planet. Sci. Lett. 304, 55–63. doi:10.1016/j.epsl.2011.01.015.

Ohuchi, T., Nishihara, Y., Seto, Y., Kawazoe, T., Nishi, M., Maruyama, G., Hashimoto, M., Higo, Y., ichi Funakoshi, K., Suzuki, A., Kikegawa, T., Irifune, T., 2015. In situ observation of crystallographic preferred orientation of deforming olivine at high pressure and high temperature. Phys. Earth Planet. Inter. 243, 1–21. doi:10.1016/j.pepi.2015.04.004.

Okaya, D.A., Christensen, N.I., 2002. Anisotropic effects of non-axial seismic wave propagation in foliated crustal rocks. Geophys. Res. Lett. 29. doi:10.1029/2001GL014285.

Russell, J.B., Gaherty, J.B., Lin, P.Y.P., Lizarralde, D., Collins, J.A., Hirth, G., Evans, R.L., 2019. High-resolution constraints on Pacific upper mantle petrofabric inferred from surface-wave anisotropy. J. Geophys. Res. Solid Earth 124, 631–657. doi:10.1029/2018JB016598.

Saruwatari, K., Ji, S., Long, C., Salisbury, M.H., 2001. Seismic anisotropy of mantle xenoliths and constraints on upper mantle structure beneath the southern Canadian Cordillera. Tectonophysics 339, 403–426.

Shapiro, N.M., Campillo, M., 2004. Emergence of broadband Rayleigh waves from correlations of the ambient seismic noise. Geophys. Res. Lett. 31, L07614. doi:10.1029/2004GL019491.

Song, T.R.A., Kawakatsu, H., 2012. Subduction of oceanic asthenosphere: evidence from sub-slab seismic anisotropy. Geophy. Res. Lett. 39, L17301. doi:10.1029/2012GL052639.

Song, T.R.A., Kawakatsu, H., 2013. Subduction of oceanic asthenosphere: A Critical Appraisal in Central Alaska. Earth Planetary Science Lett. 367, 82–94.

Takeuchi, H., Saito, M., 1972. Seismic surface waves. In *Seismology: Surface Waves and Earth Oscillations, Methods in Computational Physics*. Academic Press, New York. volume 11. pp. 217–295.

Thomsen, L., 1986. Weak elastic anisotropy. Geophysics 51, 1954–1966.

Tsvankin, I., Thomsen, L., 1994. Nonhyperbolic reflection moveout in anisotropic media. Geophysics 59, 1290–1304.

Table 1: VTI parameters for anisotropy models in Fig. 5

model name	φ^{-1}	ξ	η_κ	$a_p\,(\%)$	$a_s\,(\%)$
Millefeuille	1.013	1.105	0.917	-0.6	-5.0
A-type	1.082	1.033	0.997	-3.9	-1.6
B-type	1.033	1.016	0.999	-1.6	-0.8
C-type	0.948	0.957	0.995	2.7	2.2
E-type	1.019	1.017	1.000	-0.9	-0.9

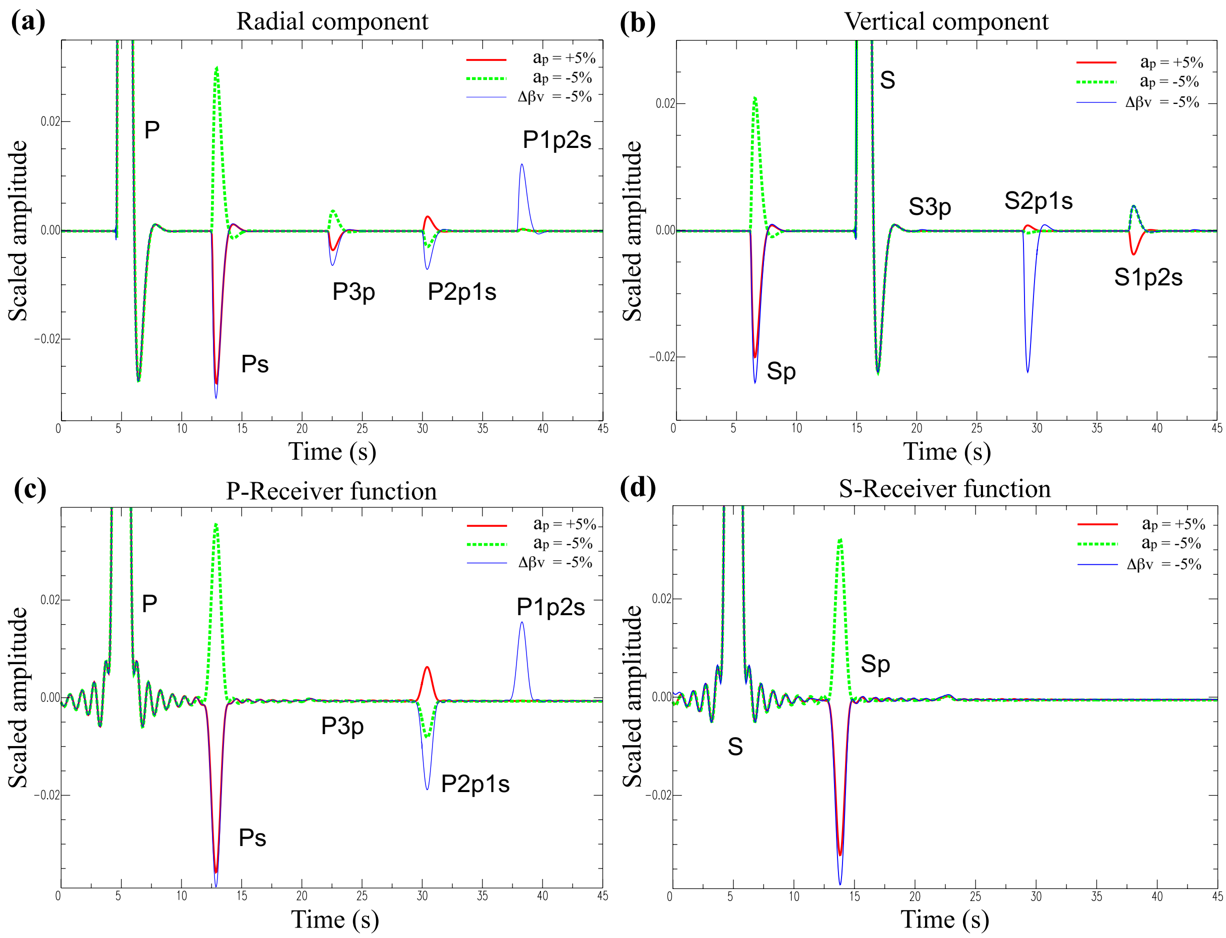

Figure 1: Synthetic elastic responses at the surface of a homogeneous isotropic layer over a homogeneous VTI half space: (a) the radial component of a plane P-wave incidence case (ray parameter: $0.06 s/km$); (b) the vertical component of a plane S-wave incidence case ($0.09 s/km$). Three cases for the half space are shown for $a_p = +5\%$ (solid line), $a_p = -5\%$ (thick broken line), and isotropic with β_V reduction of 5% (thin solid line). The amplitude is scaled with that of the main phase (i.e., P-vertical (a) and S-radial (b)) and multiplied by -1 for the S-wave case (b), and a low-pass (2s) causal Butterworth filter is applied. For multiple phases, the number of P- and/or S-legs in the upper layer are indicated. These waveforms provide essential information for receiver functions (e.g., Ammon, 1991), but corresponding receiver functions are also shown (c) for P-receiver functions and (d) for S-receiver functions; they are calculated via the spectral domain deconvolution with a water level of 0.01 and the gaussian filter coefficient $a = 2.0$; no L-Q coordinate rotation is applied. For S-receiver function, time is reversed and the amplitude is multiplied by -1 so that both receiver functions show similar primary Ps- and Sp-phase appearance. Synthetic seismograms are calculated with a locally developed Haskell matrix code for VTI. The color version of this figure is available only in the electronic edition.

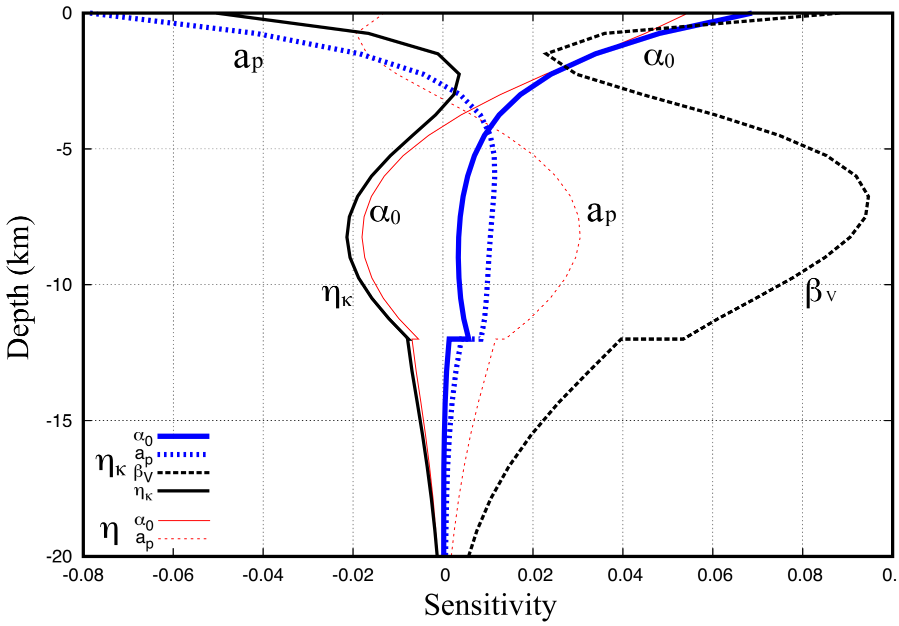

Figure 2: Partial derivatives (sensitivity kernels) for fundamental mode Rayleigh wave at a period of 7 s calculated for a flat PREM model without the water layer. The figure compares the anisotropic P-wave sensitivity for $(\alpha_H, \alpha_V, \beta_H, \beta_V, \eta_\kappa \textit{ or } \eta)$ parameter sets, where $\eta = F/(A-2L)$ is the conventional fifth parameter defined by Takeuchi and Saito (1972). Note that P-wave sensitivity is generally reduced for the η_κ case (thick solid and dotted lines) compared to the conventional η case (thin solid and dotted lines), but increased near the surface. For detail, see the text and Kawakatsu (2016b). The color version of this figure is available only in the electronic edition.

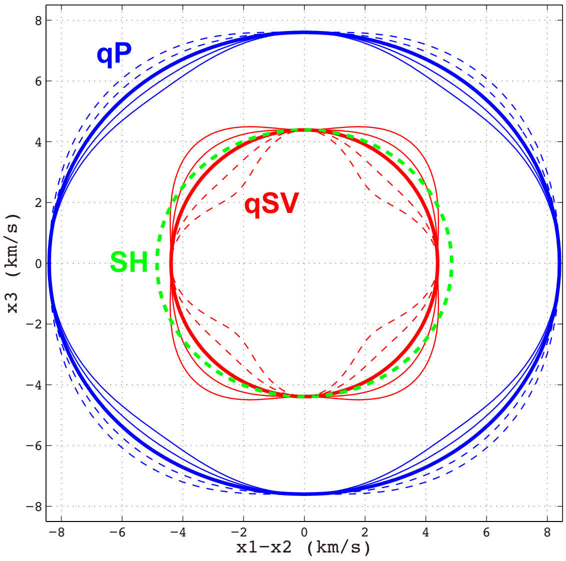

Figure 3: Phase velocity surfaces of bodywaves for five VTI models that have common P- and S-wave anisotropy ($a_p = a_s = -0.1$): outer set of five lines for quasi-P-wave, inner set of five lines for quasi-SV-wave and thick broken ellipse for SH-wave. Thick solid lines show cases when the elliptic condition is satisfied, i.e., $\eta_\kappa = 1$. Thin solid (broken) lines are for cases with $\eta_\kappa < 1$ (> 1). η_κ varies from 0.60 to 1.40 with an interval of 0.2. Note that the opposite effect of η_κ on phase velocities of q-P and q-SV. (Same as Figure 3b of Kawakatsu (2016a) but in color.) The color version of this figure is available only in the electronic edition.

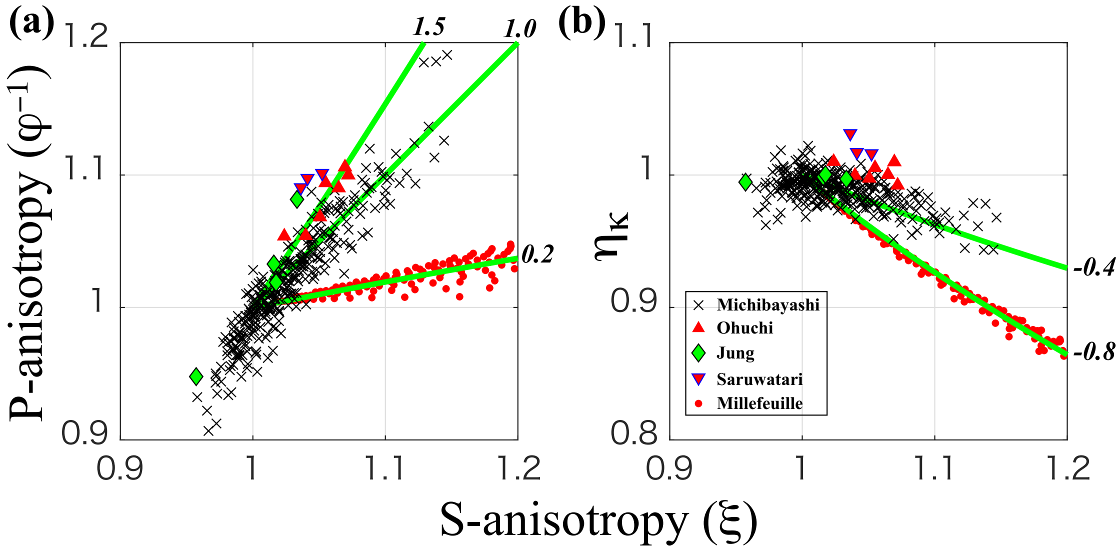

Figure 4: Correlation among the anisotropy parameters for different fabric models for some representative ones: (a) S-anisotropy (ξ) *vs.* P-anisotropy (φ^{-1}). (b) S-anisotropy *vs.* the fifth parameter (η_κ). Symbols represent fabrics of natural mantle rocks (Michibayashi et al., 2016) (cross); mantle xenolith (Saruwatari et al., 2001) (reverse triangle); laboratory rocks (Ohuchi et al., 2011, 2015) (triangle), (Jung et al., 2006) (diamond); and the millefeuille model (small solid circle). Thick lines are inferred scalings with various scaling indexes indicated by italic numbers. The color version of this figure is available only in the electronic edition.

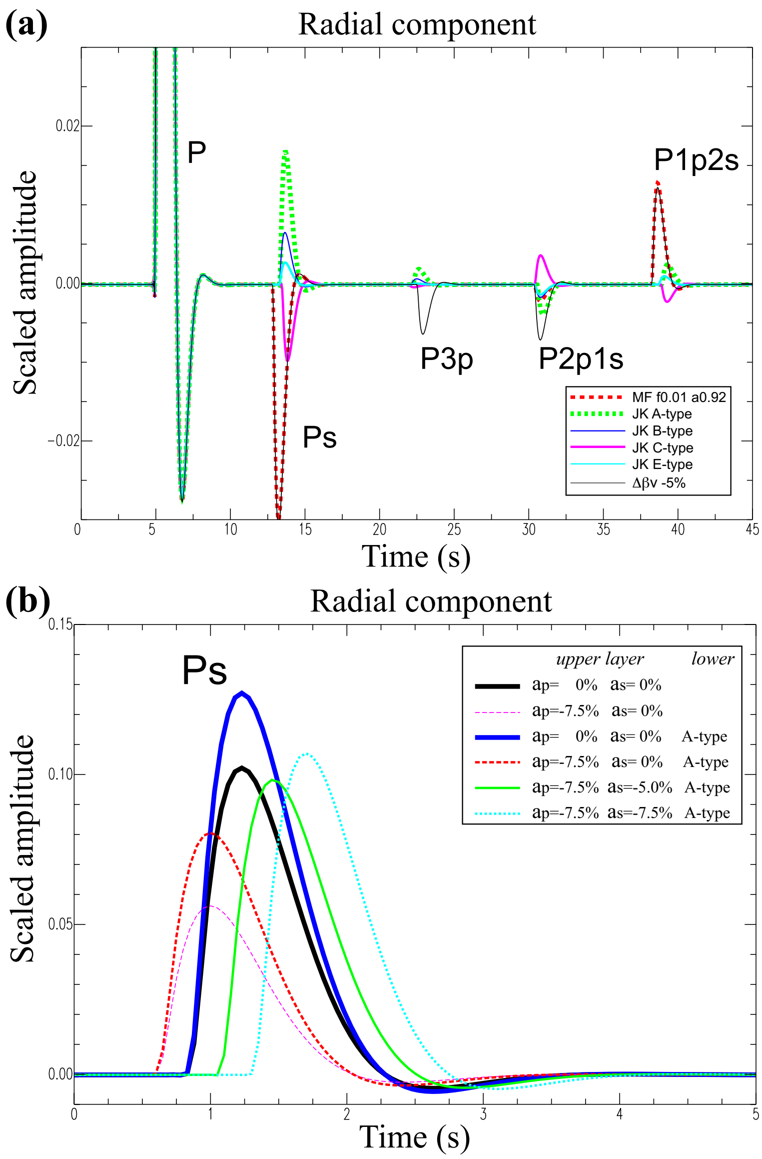

Figure 5: (a) The same as in Figure 1(a), but for various fabric models. MF stands for the millefeuille model, JK for Jung et al. (2006) fabrics (A, B, C and E-type). See the text for more details. (b) Examples of Ps phases in realistic Moho cases. The background model is the same as in Figure 1(a), but S velocity increases by 15% at the interface to simulate the Moho situation. Different lines indicate Ps phases for corresponding cases shown in the legend: (thick dark solid) both layers isotropic, (thin broken) upper layer radially anisotropic only in P-wave, lower layer isotropic, (thick medium solid; thinner broken, solid, and dotted lines) upper layer radially anisotropic as indicated in legend, lower layer radially anisotropic with that of the olivine A-type fabric (Table 1). Time 0 s corresponds to 7 s after the incident P-wave. The color version of this figure is available only in the electronic edition.

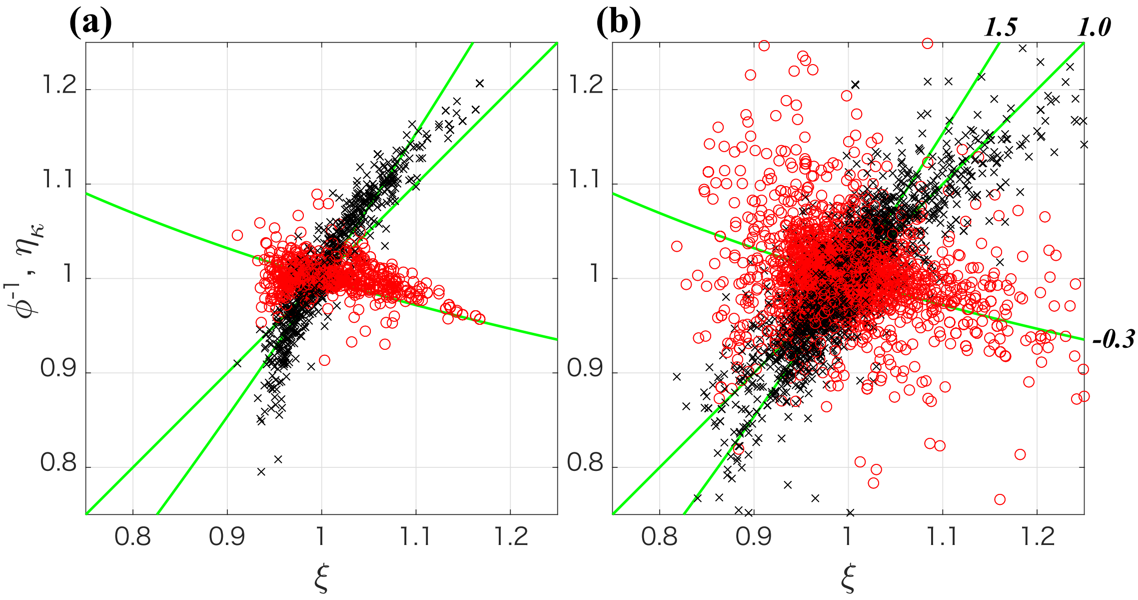

Figure 6: Correlation among the anisotropy parameters for crustal fabrics of Brownlee et al. (2017): S-anisotropy (ξ) *vs.* P-anisotropy (φ^{-1}) (cross) and S-anisotropy *vs.* the fifth parameter (η_κ) (open circle). (a) Amphibolite, and (b) the rest of fabrics. Solid lines are reference scalings with various indexes indicated by italic numbers. *cf.* Figures S1-10 for more detail. The color version of this figure is available only in the electronic edition.

Supplemental Material for “Unexpected consequences of transverse isotropy”

Hitoshi Kawakatsu[1]
[1]Earthquake Research Institute, The University of Tokyo, Japan

October 4, 2020

Contents of this file

1. Figure S1 to S10

These figures present correlations among the VTI parameters for each of the crustal fabrics reported by Brownlee et al. (2017). As similar for Figure 6 in the main text, we construct a series of VTI models for each given fabric by the azimuthal averaging of an arbitrarily rotated elastic tensor (here the rotation is done with a 15-degree interval for each Euler angle for denser sampling).

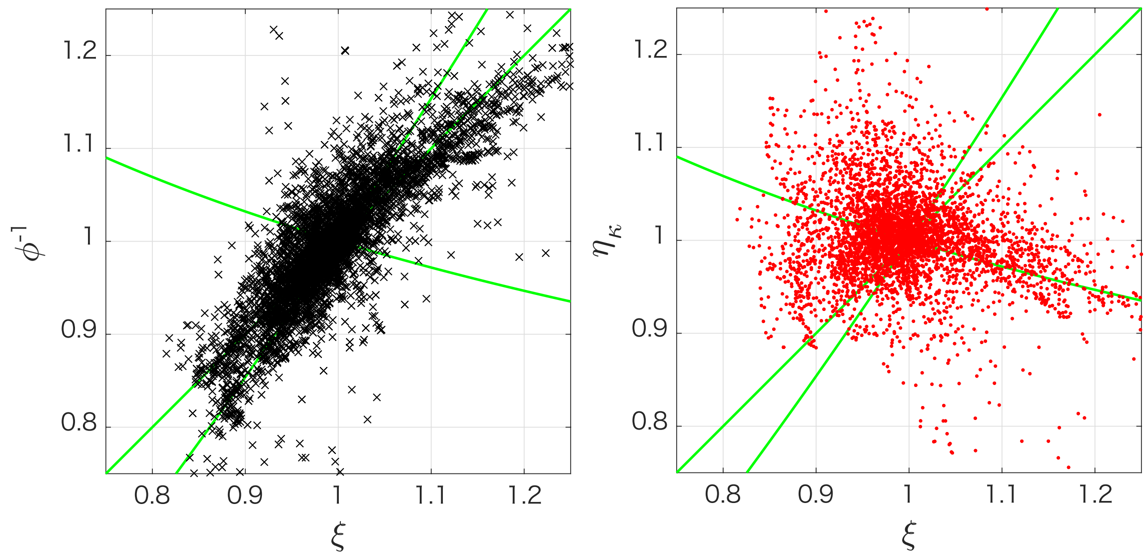

Figure S1: Correlation among the anisotropy parameters for crustal fabrics (Gneiss) of Brownlee et al. (2017): (left) S-anisotropy (ξ) *vs.* P-anisotropy (φ^{-1}) (black crosses), (right) S-anisotropy *vs.* the fifth parameter (η_κ) (red dots). Green lines are reference scalings with various indexes as in the main text.

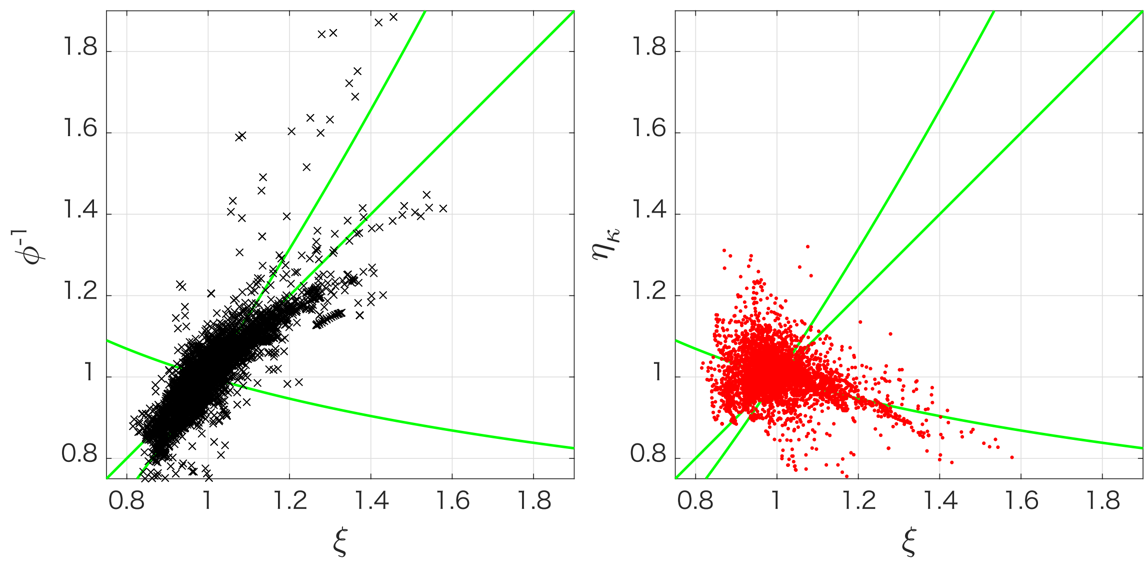

Figure S2: Same as Figure S1 but for a wider plotting range.

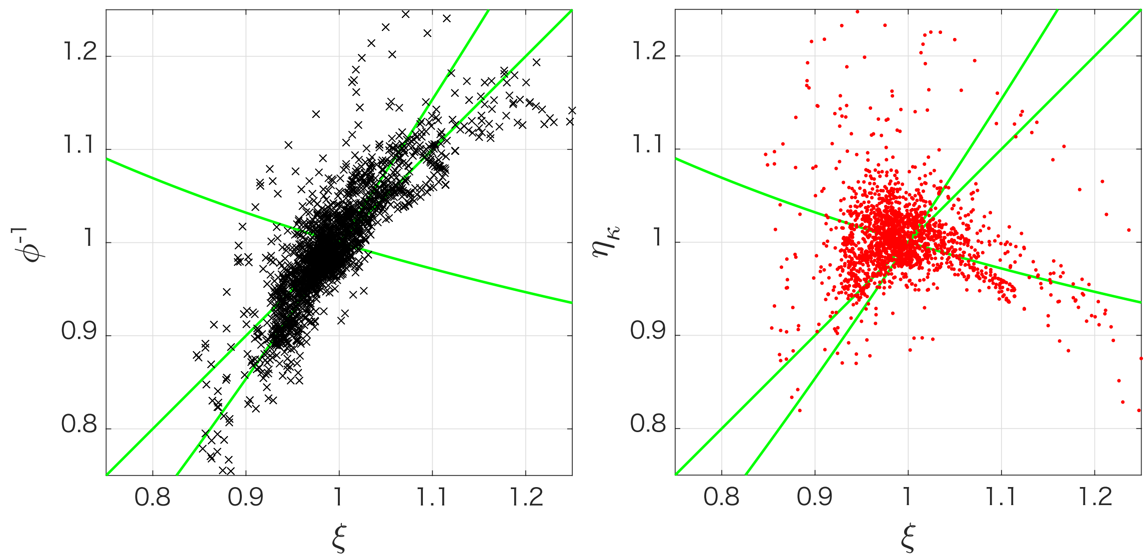

Figure S3: Same as Figure S1 but for Schist of Brownlee et al. (2017).

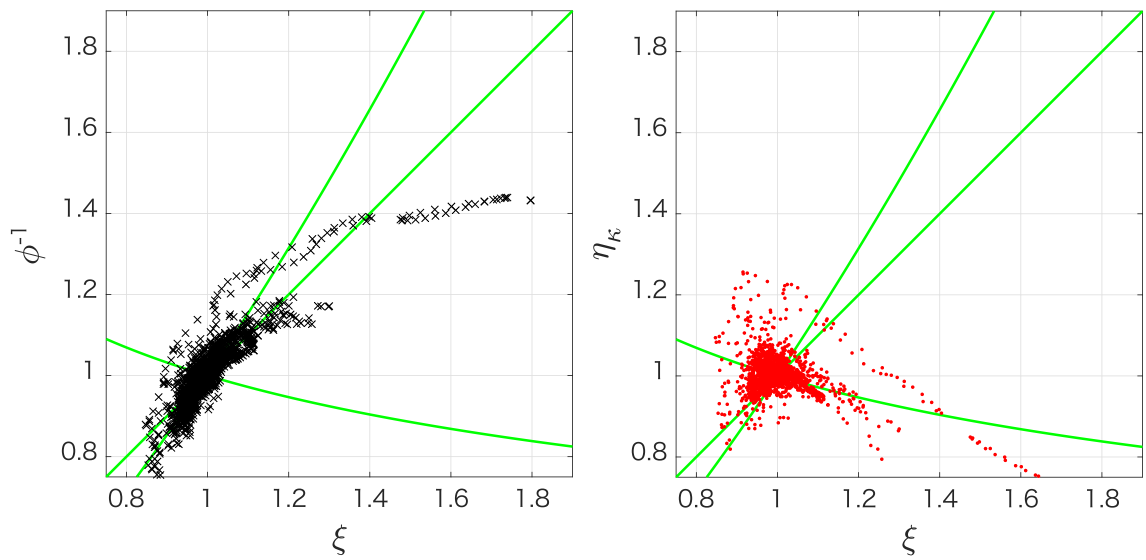

Figure S4: Same as Figure S3 but for a wider plotting range.

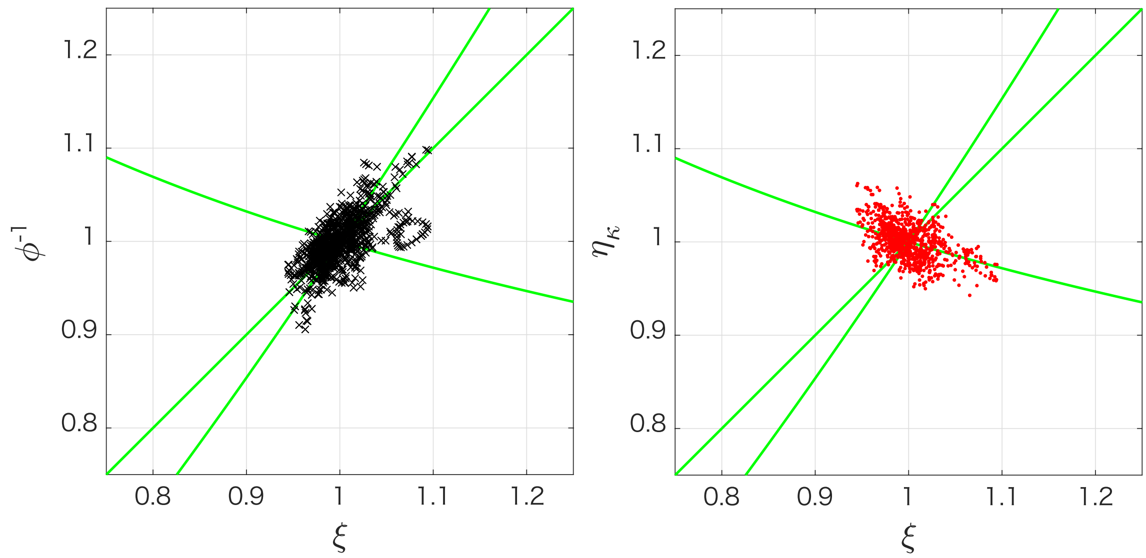

Figure S5: Same as Figure S1 but for Plutonic rocks of Brownlee et al. (2017).

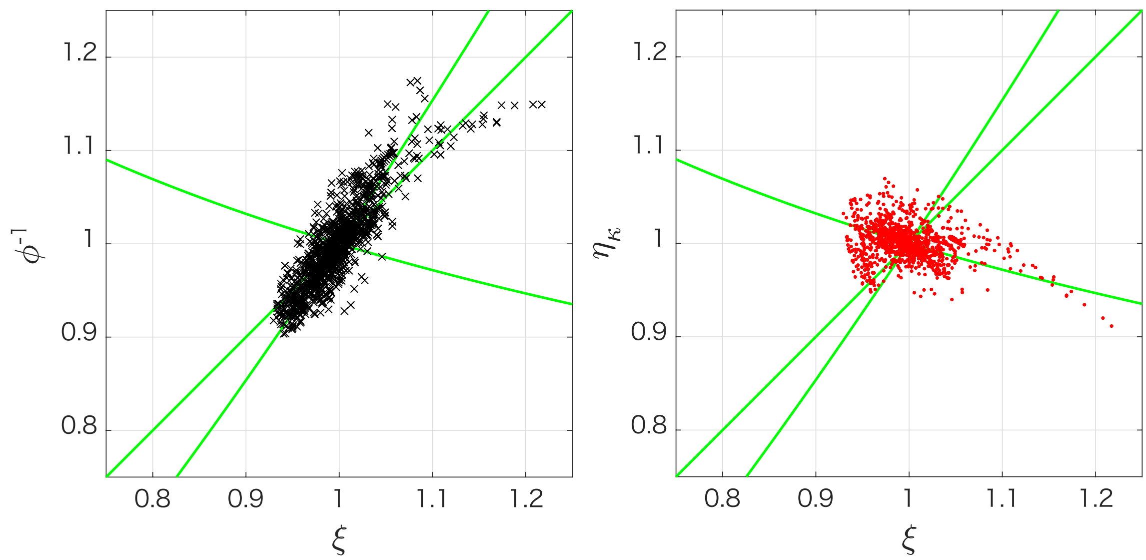

Figure S6: Same as Figure S1 but for Calcsilicate of Brownlee et al. (2017).

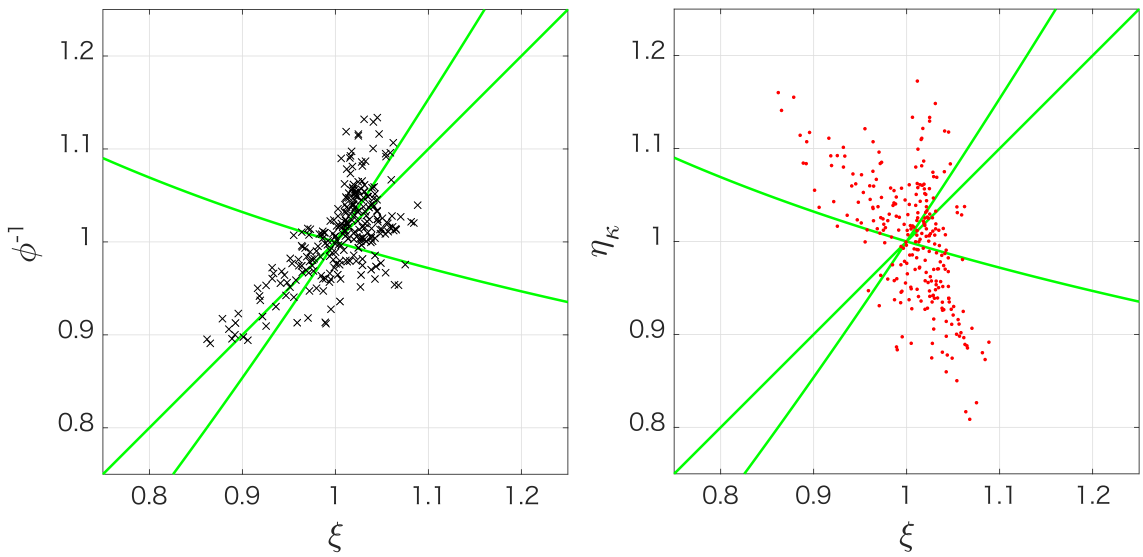

Figure S7: Same as Figure S1 but for Quartzite of Brownlee et al. (2017).

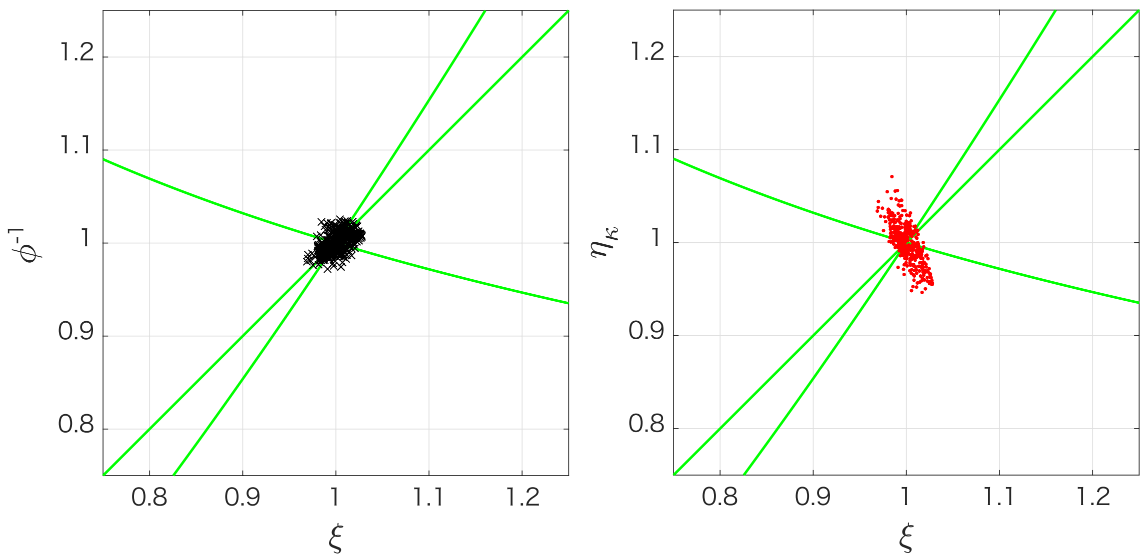

Figure S8: Same as Figure S1 but for Sandstone of Brownlee et al. (2017).

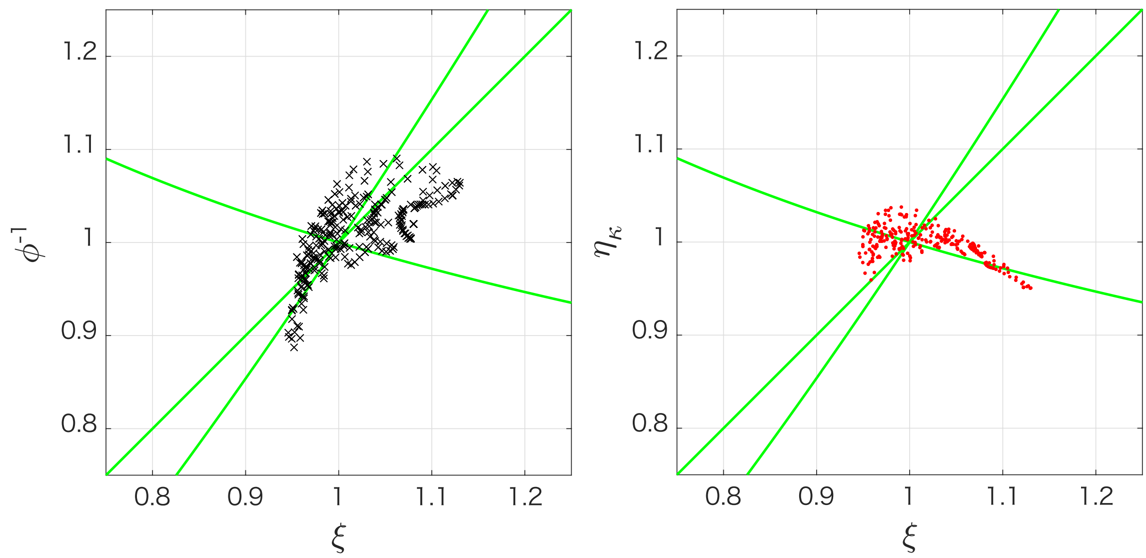

Figure S9: Same as Figure S1 but for Granfels of Brownlee et al. (2017).

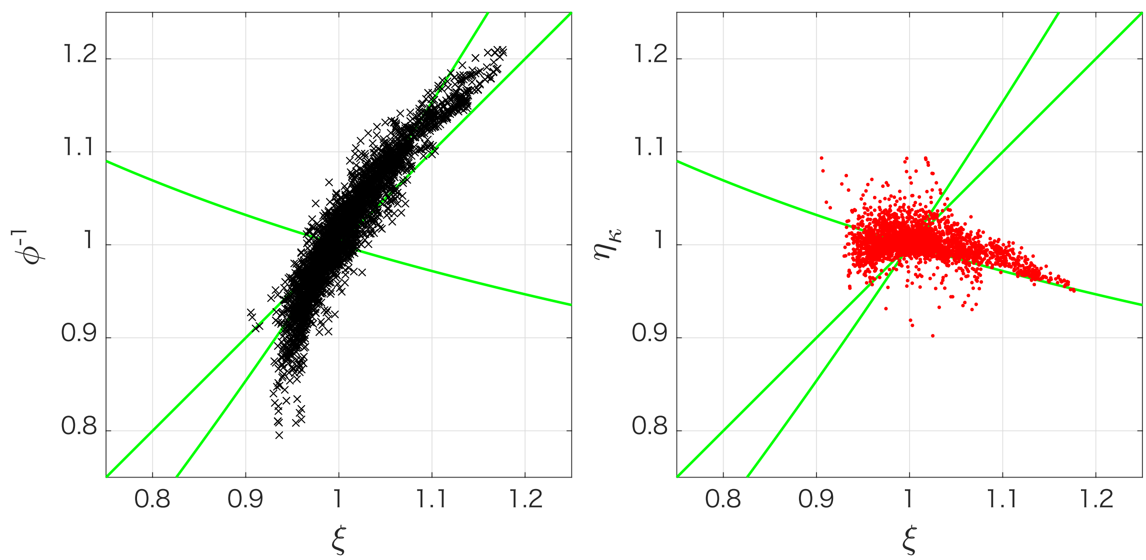

Figure S10: Same as Figure S1 but for Amphibolite of Brownlee et al. (2017).